



## Regular article

## Analysis injection area-dark current characteristics for mid-wavelength HgCdTe photodiodes

W.K. Zhang<sup>a,b</sup>, J.M. Lin<sup>a</sup>, H.L. Chen<sup>a</sup>, H. Li<sup>a</sup>, R. Wang<sup>c</sup>, R.J. Ding<sup>a,\*</sup><sup>a</sup> Key Laboratory of Infrared Imaging Materials and Detectors, Shanghai Institute of Technical Physics, Chinese Academy of Sciences, Shanghai 200083, China<sup>b</sup> University of Chinese Academy of Science, Beijing 100049, China<sup>c</sup> College of Advanced Interdisciplinary Studies, National University of Defense Technology, Changsha 410073, China

## ARTICLE INFO

## Keywords:

HgCdTe

Dark current

Injection area

Reverse welding pressure

Arrangement of common electrode

## ABSTRACT

In this paper, we study the relationship between dark current mechanism and the injection area of mid-wavelength infrared (MWIR) HgCdTe photovoltaic detectors. A simultaneous-mode nonlinear fitting program for n-on-p mid-wavelength HgCdTe infrared detectors is reported. It is found that the impact of diffusion mechanism gradually weakens and the effect of generation-recombination mechanism becomes more significant as the area of injection increasing under forward bias. The effect of trap-assisted tunneling mechanism gradually weakens as the area of injection increasing under middle reverse bias and band-to-band tunneling mechanism has less impact on dark current of MWIR HgCdTe photodiodes. And as the area of injection increasing, the effect of surface leak mechanism is gradually decrease. Finally, we find the reversed welding pressure and the arrangement of common electrode for MWIR HgCdTe Photodiodes also impacts diffusion mechanism and generation-recombination mechanism under forward bias.

## 1. Introduction

$\text{Hg}_{1-x}\text{Cd}_x\text{Te}$  (Mercury Cadmium Telluride, MCT) photodiodes have always been one of the high-performance infrared detectors because of high electron mobility, high quantum efficiency and adjustable bandgap [1,2]. The dark current restricts the performance of the MCT infrared detector that affects the noise and quantum efficiency of the device. The dark current also directly affects the detection distance of target which makes the false alarm of the infrared detection system. It can provide references for process optimization to reduce the dark current of MCT infrared detectors by analyzing dark current mechanisms [3,4]. The dark current mechanism is mainly related to substrate material defects and the process of MCT photodiodes. It can be modeled with a combination of diffusion current ( $I_{\text{diff}}$ ), generation-recombination current ( $I_{\text{gr}}$ ), trap-assisted tunneling current ( $I_{\text{tat}}$ ), and band-to-band tunneling current ( $I_{\text{bbt}}$ ) [5]. There are multiple dark current mechanisms dominated at most bias voltages for dark current of the MCT infrared detector. The non-parabolic conduction band and the effects of carrier degeneracy has great impact on the MCT device model simulation. Z.J. Quan builds the new MCT device model which takes account of carrier degeneracy and conduction band non-parabolicity to analyze characteristics of long-wavelength MCT n-on-p photodiodes [6–8]. The non-uniformity is a major issue in large area IR detector arrays of

HgCdTe. R.S. Saxena presents the effect of variations in the various device and material parameters on the performance of MWIR MCT photodiodes [9]. Temperature also has great impact on the dominant of dark current mechanism [10,11]. The area of injection impacts the contact of PN junction and affects electron mobility which influence the width and electric field of space charge region. Therefore, it is great significance to study the relationship between the area of injection and the components of dark current mechanism.

In this paper, we research the relationship between the area of injection and dark current mechanism of the MWIR HgCdTe photodiodes by new MCT device fitting-model using the R-V curves measured. By studying the p-V curves, it is found that the slope of p-V curve near the zero-bias decreases for DIFF mechanism and the slope of p-V curves has great variation for GR mechanism under small reverse bias. And we find that it is caused by the reversed welding pressure and arrangement of common electrode for MWIR HgCdTe photodiodes.

## 2. Theoretical models

The dark current mechanism of MCT photodiodes is modeled with the combination of diffusion (DIFF) current, generation-recombination (GR) current, trap-assisted-tunneling (TAT) current, and band-to-band tunneling (BBT) current. The surface leakage currents and the

\* Corresponding author.

E-mail addresses: [zhangwukang14@mails.ucas.ac.cn](mailto:zhangwukang14@mails.ucas.ac.cn) (W.K. Zhang), [dingrj@mail.sitp.ac.cn](mailto:dingrj@mail.sitp.ac.cn) (R.J. Ding).

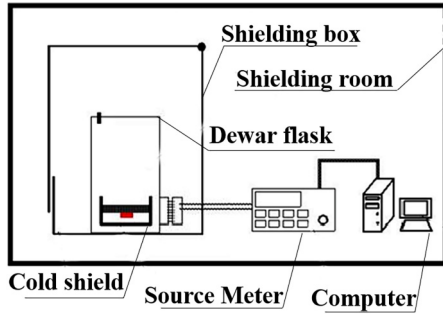


Fig. 1. MCT infrared detector I-V test platform.

Table 1

Material and device parameters of I–VI photovoltaic samples.

Sample number	I	II	III	IV	V	VI
$x$	0.3049	0.3033	0.3048	0.3034	0.2986	0.3007
$A \times 10^{-5} \text{ (cm}^2\text{)}$	10.0	40.0	78.4	96.0	78.4	40.0
$N_a \times 10^{15} \text{ (cm}^{-3}\text{)}$	6.63	6.01	8.91	9.01	6.75	6.48
$\mu_p \text{ (cm}^2\text{/Vs)}$	441.9	363.5	466.9	451.3	554.2	477
$f \text{ (kg/s)}$	2.5	2.5	2.0	1.5	1.7	2.5

dislocations in the material, which intersect the junction, are generally held responsible as a possible source of ohmic current. Taking series resistance  $R_s$  into account, the total resistance  $R_{exp}$  generated by the measured dark current can be expressed as [6,7,12]:

$$R_{exp} = \left( \frac{1}{R_{diff}} + \frac{1}{R_{gr}} + \frac{1}{R_{lat}} + \frac{1}{R_{bbt}} + \frac{1}{R_{shunt}} \right)^{-1} + R_s \quad (1)$$

$R_{diff}$ ,  $R_{gr}$ ,  $R_{lat}$ ,  $R_{bbt}$  respectively indicates the corresponding resistance generated by the four mechanisms of dark current.  $R_{shunt}$  is the diodes shunt resistance. The resistance  $R_{diff}$  generated by diffusion current is given as [13–15]:

$$R_{diff} = \left( \frac{dI_{diff}}{dV_e} \right)^{-1} = \left[ A J_{diff0} \frac{q}{kt} \exp\left(\frac{qV}{kt}\right) \right]^{-1} \quad (2)$$

$J_{diff0}$  is given as:

$$J_{diff0} = q n_i^2 \sqrt{\frac{kt}{q}} \left( \sqrt{\frac{\mu_n}{\tau_n}} \frac{1}{N_a} + \sqrt{\frac{\mu_p}{\tau_p}} \frac{1}{N_d} \right) \quad (3)$$

Here  $A$  is the area of injection;  $n_i$  is the intrinsic carrier concentration;  $\mu_n$  and  $\mu_p$  represent the electron and hole mobility respectively;  $\tau_p$  and  $\tau_n$  represent the lifetime of minority carriers in the n and p region;  $N_a$  and  $N_d$  represent the dopant density in the p and n region respectively;  $q$  is the quantity of electric charge;  $k$  and  $T$  represent the Boltzmann constant and the temperature respectively; The bias voltage is an effective bias  $R_e = V - IR_s$  corrected by the series resistance  $R_s$ . Here,  $V$  is the applied voltage and  $I$  is the total dark current.

The resistance  $R_{gr}$  generated by generation-recombination current is given as [13,16]:

$$R_{gr} = \left( \frac{dI_{gr}}{dV_e} \right)^{-1} = \frac{\tau_0 \sqrt{V_{bi}}}{A 2 n_i w_0 k T} \left[ \frac{\cosh\left(\frac{qV}{2kT}\right) \frac{qV}{2kT} f(b) + \sinh\left(\frac{qV}{2kT}\right) \frac{df(b)}{dV} + \frac{\sinh\left(\frac{qV}{2kT}\right) f(b)}{2(V_{bi}-V)^{\frac{3}{2}}} \right]^{-1} \quad (4)$$

Here  $\tau_0$  and  $W_0$  respectively represent the effective lifetime in the depletion region and the width of the depletion region under the zero bias;  $V_{bi}$  is the build-up potential inside PN junction.  $f(b)$  can be expressed

as:

$$f(b) = \begin{cases} \frac{\ln(b + \sqrt{b^2 - 1})}{\sqrt{b^2 - 1}} & b > 1 \\ \frac{1}{b} & b = 1 \\ \frac{1}{\sqrt{1 - b^2}} \left[ \frac{\pi}{2} - \arctan\left(\frac{b}{\sqrt{1 - b^2}}\right) \right] & b < 1 \end{cases} \quad (5)$$

$b$  is given as:

$$b = \exp\left(\frac{-qV}{2kT}\right) \cosh\left[\frac{E_t - E_i}{kT} + \frac{1}{2} \ln\left(\frac{\tau_p}{\tau_n}\right)\right] \quad (6)$$

here  $E_t$  and  $E_i$  represent the trap energy level and the intrinsic Fermi energy level respectively.

The resistance  $R_{bbt}$  generated by band-to-band tunneling current is given as [13,17]:

$$R_{bbt} = \left( \frac{dI_{bbt}}{dV_e} \right)^{-1} = \left[ bbt_1 (-1.5 \sqrt{V_{bi} - V} + 0.5) \exp\left(-\frac{bbt_2}{\sqrt{V_{bi} - V}}\right) \right]^{-1} \quad (7)$$

$bbt_1$  can be expressed as:

$$bbt_1 = -A \frac{q^3 \sqrt{2m_e}}{4\pi^3 \hbar^2 \sqrt{E_g}} \sqrt{\frac{q N_a N_d}{2\epsilon_s \epsilon_0 (N_a + N_d)}} \quad (8)$$

$bbt_2$  can be expressed as:

$$bbt_2 = -\frac{\pi \sqrt{\frac{m_e}{2}} E_g^{\frac{3}{2}}}{2q\hbar} \sqrt{\frac{2\epsilon_s \epsilon_0 (N_a + N_d)}{q N_a N_d}} \quad (9)$$

Here  $m_e$  and  $E_g$  represent the electron effective mass and the band gap respectively;

The resistance  $R_{lat}$  generated by trap-assisted tunneling current is given as [13,18,19]:

$$R_{lat} = \left( \frac{dI_{lat}}{dV_e} \right)^{-1} = \left[ -tat_1 \exp\left(\frac{tat_2}{\sqrt{V_{bi} - V}}\right) \left( 1 - \frac{tat_2}{2\sqrt{V_{bi} - V}} \right) \right]^{-1} \quad (10)$$

The  $tat_1$  can be expressed as:

$$tat_1 = -\frac{A \pi^2 q^2 N_t m_e M^2}{h^3 (E_g - E_t)} \quad (11)$$

And  $tat_2$  can be expressed as:

$$tat_2 = -\frac{\sqrt{3} E_g^{\frac{3}{2}} F(a)}{8\sqrt{2} q P} \sqrt{\frac{2\epsilon_s \epsilon_0 (N_a + N_d)}{q N_a N_d}} \quad (12)$$

The  $F(a)$  is given as:

$$F(a) = \frac{\pi}{2} \sin^{-1}(1-2a) + 2(1-2a) \sqrt{a(1-a)}, \quad a = \frac{E_t}{E_g} \quad (13)$$

Here  $M$  and  $P$  represent the transition matrix element and Kane matrix element respectively. The  $N_t$  represents defect concentration in the depleted region.

The diodes shunt resistance  $R_{shunt}$  generated by excess current component is given as:

$$R_{shunt} = \frac{V_e}{I_{sh}} \quad (14)$$

Here the  $I_{sh}$  is an Ohmic current. The surface leakage currents and the dislocations in the material that intersect the junction are generally held responsible as a possible source for this part of excess current. For the diodes with small leakage current, the highest value of dynamic resistance may be assumed as the shunt resistance of the diode.

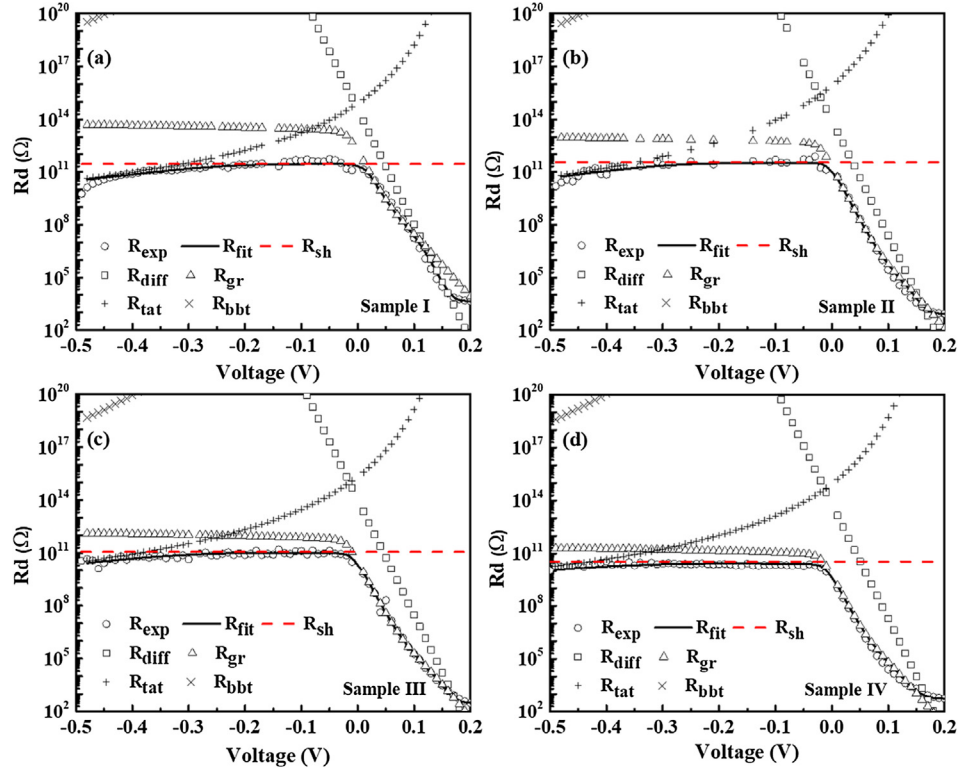


Fig. 2. Measured R-V curves and their fitting results for I-IV devices.

**Table 2**  
Fitting parameters of I-IV devices.

Sample	$N_d$ (cm <sup>-3</sup> )	$\tau_n$ (ns)	$\tau_0$ (ns)	$N_t$ (cm <sup>-3</sup> )	$R_{shunt}$ (Ω)	$\frac{E_t}{E_g}$
Sample I	$4.39 \times 10^{16}$	0.122	0.730	$3.67 \times 10^{12}$	$2.31 \times 10^{11}$	0.440
Sample II	$3.96 \times 10^{16}$	0.325	0.079	$6.18 \times 10^{12}$	$2.23 \times 10^{11}$	0.386
Sample III	$1.24 \times 10^{16}$	0.513	0.051	$1.76 \times 10^{12}$	$3.32 \times 10^{11}$	0.397
Sample IV	$1.12 \times 10^{16}$	0.554	0.017	$1.41 \times 10^{12}$	$3.21 \times 10^{10}$	0.424

The simulation of the device model uses non-linear fitting. There are six fitting parameters to be extracted from R-V curves as follows: the dopant density  $N_d$  in the n region, the lifetime of electrons  $\tau_n$  in the p region, the effective lifetime  $\tau_0$  in the depletion region, the relative energy position of trap level  $\frac{E_t}{E_g}$  and the trap density  $N_t$  in the depletion region, and the shunt resistance  $R_{shunt}$ . Within the range of the characteristic parameters, a theoretical R-V fitting curve is obtained for each set of parameters. Finally, the theoretical fitting value  $R_{fit}$  and the

experimental data  $R_{exp}$  are used to calculate the value of function  $F$ . And  $F$  can be expressed as [20]:

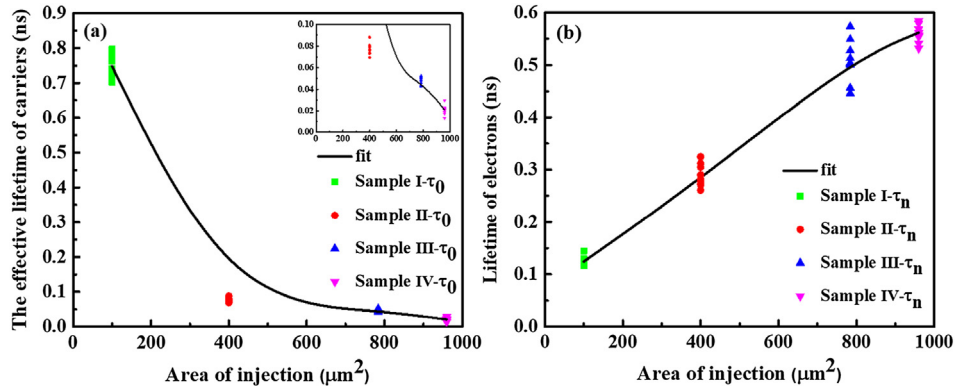
$$F = \sum_{n=1}^N [\log(R_{fit}(V)) - \log(R_{exp}(V))]^2 \quad (15)$$

Here  $N$  is the number of data. The fitting parameters which are corresponding to the smallest  $F$  are extracted as device parameters. In order to analyze change of the dark current mechanism, we use p function to describe components of dark current mechanism. And the function  $p$  can be expressed as:

$$p = \frac{R_{fit} - R_s}{R_x} \quad (16)$$

Here  $R_x$  can be replaced by  $R_{diff}$ ,  $R_{gr}$ ,  $R_{tat}$ ,  $R_{bbt}$  and  $R_{shunt}$ . The range of  $p$  value is 0–1.

The simulation is solved by using simulated annealing (SA) and genetic algorithm (GA). Because of the stronger local search for SA and the better overall search convergence for GA, this combined algorithm

Fig. 3. The trend of  $\tau_0$  and  $\tau_n$  with four different area of injection from 40 MWIR HgCdTe photodiodes.

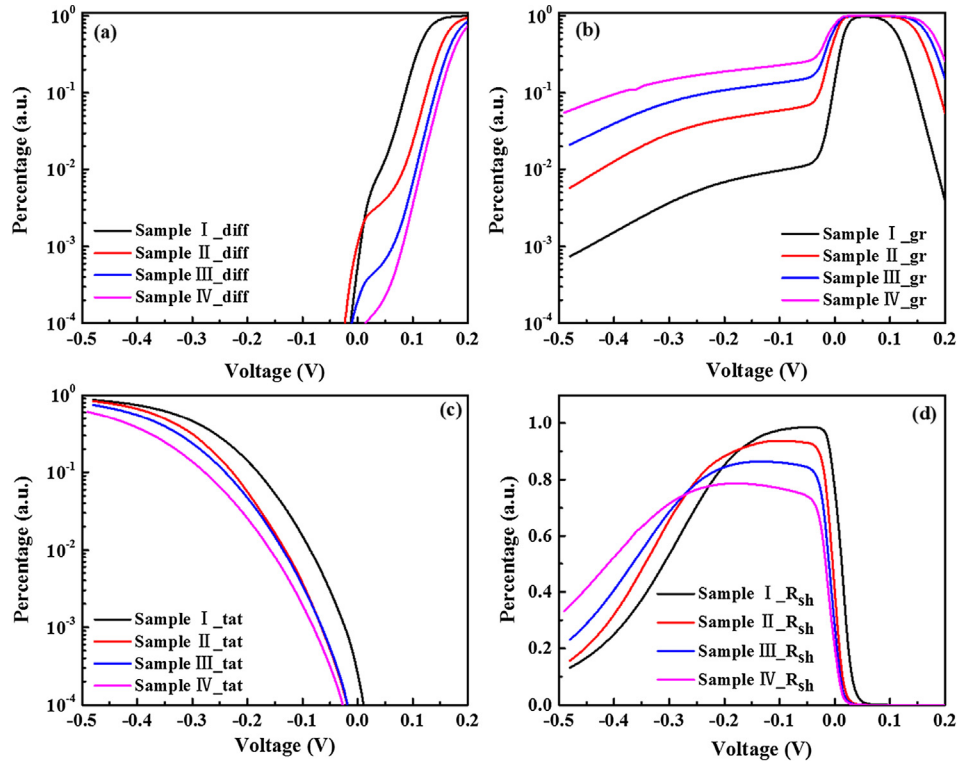


Fig. 4. Four dark current mechanisms p-V curve for I-IV devices.

can improve the solutions quality. An initial value of the six parameters can be estimated by the method described in Quan work [7]. The range of parameters is set by referring to the initial values of the six parameters. Finally, we use the SA-based GA algorithm to minimize the target F function.

### 3. Results and discussion

The mid-wavelength MCT infrared photovoltaic detectors use the liquid-phase epitaxy (LPE) process to grow p-type  $\text{Hg}_{1-x}\text{Cd}_x\text{Te}$ . The  $n^+$ -on-p diodes are fabricated by boron ion implantation. It is necessary to

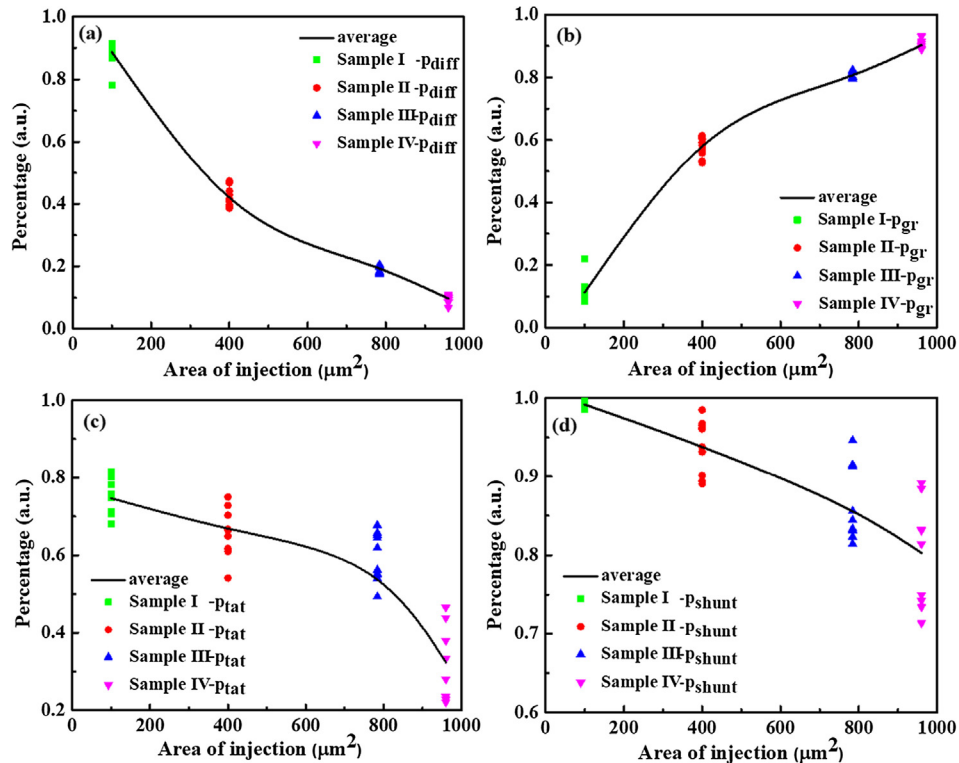


Fig. 5. The uniformity of four dark current mechanisms p-V curve for I-IV devices.

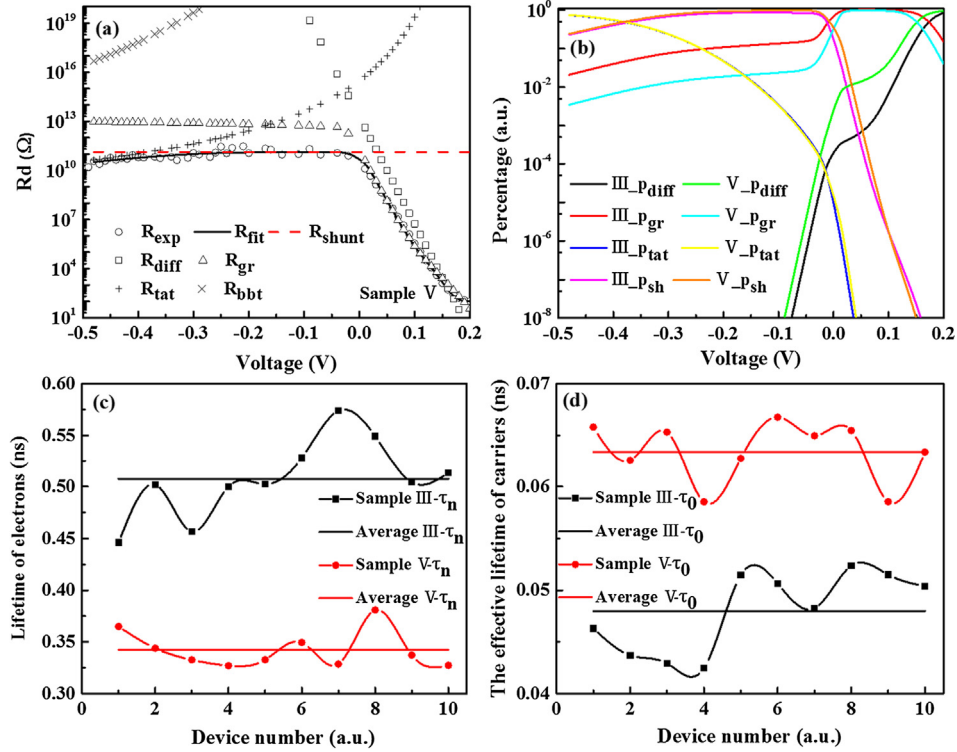


Fig. 6. The fitting results for III and V devices.

package the devices in the high-vacuum dewar flask before I-V testing at liquid nitrogen temperature. The I-V test platform uses the Keithley 6430 micro-current meter, and the accuracy of micro-current meter can reach pA level. Fig. 1 is I-V test platform, and it can reduce the measurement noise which is made by the external vibration and electromagnetic waves. Firstly, we analyze the impact of the area of injection on dark current mechanism components by fitting the R-V curves of I-IV devices. All diodes are fabricated in different epitaxial layer. The parameters of I-VI devices are shown in Table 1, where  $x$  is the Cd composition,  $A$  is the area of injection and  $f$  is the reversed welding pressure. The temperature of I-V test is 77 K.

The fitting results of I-IV devices are shown in Fig. 2. Fig. 2(a)–(d) correspond to the R-V fitting of I-IV devices, and consistent with the effects of four dark current mechanism components under different biases. It can be seen in Fig. 2 that  $R_{bbt}$  contributes very small and  $R_{lat}$  becomes dominant under reverse bias.  $R_{gr}$  and  $R_{shunt}$  has the large contribution near zeros forward bias.  $R_{diff}$  dominates the total dynamic resistance under large forward bias. The fitting parameters are listed in Table 2 for I-IV devices. It can be seen from Table 2 that the value of  $\tau_0$  decreases and the value of  $\tau_n$  enhance as the area of injection increasing.

We fit the R-V curves of 40 MWIR HgCdTe photodiodes to rule out chance and see the non-uniformity of diodes in HgCdTe arrays. The each number of diodes which the area of injection same to I-IV diodes is 10. The trend of  $\tau_n$  and  $\tau_0$  with four different area of injection from 40 diodes are shown in Fig. 3, and the small figure on the Fig. 3 upper right is local enlarged drawing. It can be seen that the trend of  $\tau_0$  decreases and the trend of  $\tau_n$  increases as the area of injection increasing for most diodes. As the area of injection increasing, more carriers diffuse to N and P region and the rate of carrier recombination will increase. On the other hand, we think large area of injection will decrease built in electrical field under the same bias. It enhances the rate of carrier recombination in the depletion region to decrease the injection of minority carriers in PN junction. When built in electrical field increasing, the carriers in the depletion region will be too late to make recombination and driven away by the electric field. The fitting

parameter  $\tau_n$  is smaller [21] because the forward current is dominated by the GR current in the depletion region at low temperatures, resulting in a very large error for the extracted parameter  $\tau_n$  [12]. So the value of  $\tau_n$  can be seen as references to analysis trends of  $\tau_n$ . Generally, the measured carrier lifetime of electron in the p region is about several nanoseconds.  $\tau_0$  will be reduced in the strong built-in field region due to absent of screen effect on electrical traps and deep level resonant scattering in depletion region [6]. Therefore, it is possible that  $\tau_0$  is less than the carrier lifetime in the p region.

In order to study the relationship between four dark current mechanisms and the area of injection for MWIR HgCdTe photodiodes, we analyze the p-V curves of I-IV devices which are shown in Fig. 4. The BBT mechanism has less impact on dark current of MWIR HgCdTe photodiodes. So we analyze the p-V curves of DIFF, GR, TAT and ohmic current mechanism in Fig. 4. For Fig. 4(a) and (b), it can be seen that p value decreases for DIFF mechanism and increases gradually for GR mechanism as the area of injection increasing under large forward bias. For Fig. 4(c), we can find that the p decreases for TAT mechanism as the area of injection increasing under middle reverse bias. For the expressions of  $R_{diff}$  and  $R_{gr}$ , we can know  $p_{diff} \propto \sqrt{\frac{1}{\tau_n}}$  and  $p_{gr} \propto \frac{1}{\tau_0}$ . So the trend of  $p_{diff}$  and  $p_{gr}$  is fitted the expressions. For the decreasing of  $p_{lat}$ , we think large area of injection will decrease built in electrical field under the same bias to make the effect of TAT mechanism decrease. Because carriers in trap energy also can produce TAT current under built in electrical field. For Fig. 4(d), it can be seen that p value of  $R_{shunt}$  decreases as the area of injection increasing under small reverse bias. The parameter  $p_{sh}$  also can represent the effect of the surface leakage currents. For the decreasing of  $p_{sh}$ , it can be explained that the effect of

**Table 3**  
Fitting parameters of V device.

Sample	$N_d$ (cm <sup>-3</sup> )	$\tau_n$ (ns)	$\tau_0$ (ns)	$N_t$ (cm <sup>-3</sup> )	$R_{shunt}$ (Ω)	$\frac{E_t}{E_g}$
Sample V	$3.12 \times 10^{16}$	0.365	0.065	$1.60 \times 10^{12}$	$1.33 \times 10^{11}$	0.359



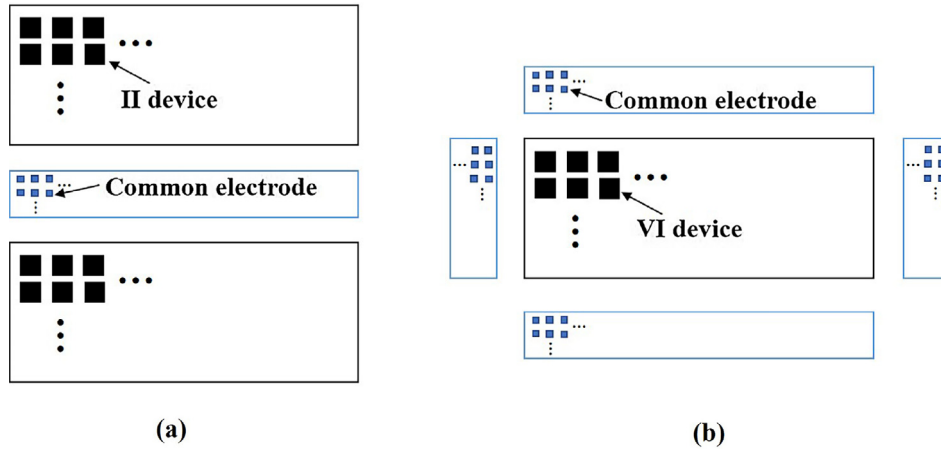


Fig. 7. Arrangements of the common electrodes for II and VI devices.

surface leakage mechanism become increasingly prominent as the area of injection decreasing. In Fig. 4, It is found that slope of p-V curve near the zero-bias decreases for DIFF mechanism and slope of p-V curves has great variation for GR mechanism under small reverse bias. This may be due to the influence of stress on the device surface, junction defect density, and device connection during the reverse soldering process. And  $R_s$  is not just constant which also can influence slope of p-V curve for DIFF mechanism. The array structure of the device affects the arrangement of the common electrodes to make  $R_s$  changed.

In Fig. 5, we also fit the R-V curves of 40 MWIR HgCdTe photodiodes and the each number of diodes which the area of injection similar to I–IV diodes is 10. Fig. 5(a), (b) is the relationship between p and the area of injection with 0.15 V supply voltage for DIFF and GR mechanism respectively. Fig. 5(c) is relationship between p and the area of injection with  $-0.4$  V supply voltage for TAT mechanism. Fig. 5(d) is relationship between p and the area of injection with

$-0.05$  V supply voltage for ohmic current mechanism to estimate affection of surface leak current. As we can see in Fig. 5, the trend of  $p_{diff}$  is decreasing for DIFF mechanism and the trend of  $p_{gr}$  is gradually increasing for GR mechanism as the area of injection increasing with 0.15 V supply voltage for 40 MWIR HgCdTe photodiodes. For TAT mechanism and ohmic current mechanism, the trend of  $p_{tat}$  and  $p_{sh}$  are gradually decreasing as the area of injection increasing for 40 MWIR HgCdTe photodiodes.

In order to analyze the relationship between reversed welding pressure and dark current mechanism, we fit the R-V curves of III and V device with the same area of injection and different reversed welding pressures. The fitting results are show in Fig. 6 and Table 3. It can be seen from Table 1 that the reversed welding pressure of III device is 2.0 kg/s and V device is 1.7 kg/s. In order to rule out chance, we also fit the R-V curves of 10 devices similar to III and 10 devices similar to V. In Fig. 6, (a) is R-V fitting of V devices. Fig. 6(b) is p-V curve of III and V

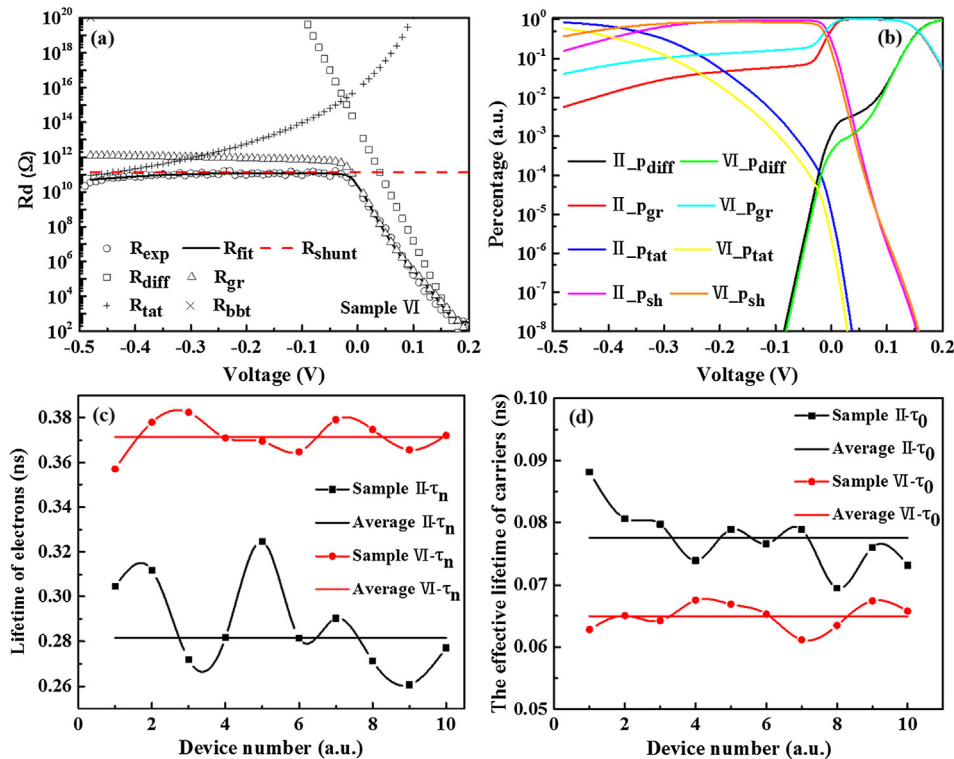


Fig. 8. The fitting results for II and VI devices.

**Table 4**  
Fitting parameters of VI device.

Sample	$N_d$ (cm <sup>-3</sup> )	$\tau_n$ (ns)	$\tau_0$ (ns)	$N_t$ (cm <sup>-3</sup> )	$R_{shunt}$ ( $\Omega$ )	$\frac{E_t}{E_g}$
Sample VI	$1.33 \times 10^{16}$	0.379	0.061	$1.49 \times 10^{12}$	$1.35 \times 10^{11}$	0.434

devices. In Fig. 6(b), it can be seen that the slope of V device of p-V curve for DIFF mechanism is smaller than III device near zero forward bias, and the slope of V device of p-V curve for GR mechanism is higher than III device under backward bias and large forward bias. Fig. 6(c) and (d) show that the average  $\tau_n$  of V devices decreases compare with III device and the average  $\tau_0$  of V devices is higher than III device. This can be explained that the stress during the reflow process affects device surface and the defect density of the junction area. Stress can affect dark current by generating piezoelectric effects, changing the band gap and changing defects defect performance.

The distribution of common electrodes may also affects the component of DIFF mechanism. We fit the R-V curves of two devices with the same implant area and same reversed soldering pressures. But the arrangement of the common electrodes of two devices is different. As shown in Fig. 7, Fig. 7(a) is the arrangement of the common electrodes of II device and Fig. 7(b) is the arrangement of the common electrodes of VI device. The arrangement of the common electrodes of Fig. 7(a) is considered for using short wave in MWIR HgCdTe photodiodes. In order to rule out chance, we also fit the R-V curves of 10 devices similar to II and 10 devices are similar to VI. The fitting result is shown in Fig. 8 and Table 4. Fig. 8(a) is R-V fitting of VI device. Fig. 8(b) is p-V curve of II and VI devices. It can be seen that the slope of VI device of p-V curve for DIFF mechanism near zeros forward bias is higher than II device and the slope of p-V curve for GR mechanism is lower than II device under small forward bias. Fig. 8(c) and (d) show that the average  $\tau_n$  of II device decreases compare with VI device and the average  $\tau_0$  of II device is higher than VI device. It can be explained that the common electrode will change series resistant and have an impact on the working voltage of MWIR HgCdTe photodiodes to make the built in electrical field changed. DIFF mechanism fails to become the dominant dark current due to the series resistance effect.

#### 4. Conclusion

A data-processing method is developed to obtain the device parameters from R-V curves measured on MWIR HgCdTe n-on-p photodiodes. By studying the R-V curves of four middle-wavelength devices with the different injection area, we find that the impact of diffusion mechanism gradually weakens and the effect of generation-recombination mechanism becomes more significant as the area of injection increasing under forward bias. The effect of TAT mechanism gradually weakens as the area of injection increasing under middle reverse bias and BBT mechanism has less impact on dark current of MWIR HgCdTe photodiodes. And as the area of injection increasing, the effect of surface leak mechanism is gradually decrease. By studying the p-V curves, it is found that slope of p-V curve near the zero-bias decrease for DIFF mechanism and the slope of p-V curves has great variation for Gr mechanism under small reverse bias. We find it is caused by the reversed welding pressure and the arrangement of common electrodes. This can be explained that the stress during the reflow process affects device surface and the defect density of the junction area. Stress can affect dark current by generating piezoelectric effects,

changing the band gap and changing defects defect performance. The common electrode will change contact resistant that will have an impact on the working voltage of MWIR HgCdTe photodiodes to make the built in electrical field changed which will impacts DIFF and GR mechanism under forward bias.

#### Conflict of interest

None.

#### Acknowledgement

This work was supported by Hunan Provincial Key Laboratory of High Energy Laser Technology (Num: GNJGJS01).

#### References

- [1] G. Hansen, J. Schmit, Calculation of intrinsic carrier concentration in  $Hg_{1-x}Cd_xTe$ , *J. Appl. Phys.* 54 (3) (1983) 1639–1640.
- [2] A. Rogalski, Infrared detectors: an overview, *Infrared Phys. Technol.* 43 (3–5) (2002) 187–210.
- [3] F. Juang, Y. Su, S. Chang, S. Chang, C. Chiang, Y. Cherng, Analysis of the dark current of focal-plane-array  $Hg_{1-x}Cd_xTe$  diode, *Mater. Chem. Phys.* 64 (2) (2000) 131–136.
- [4] H. Yuab, X. Yang, F. Tong, Dark current analysis of SWIR HgCdTe photovoltaic detectors, *Semicond. Sci. Technol.* 8 (5) (1993) 700–704.
- [5] V. Gopal, W. Qiu, W. Hu, Modelling of illuminated current-voltage characteristics to evaluate leakage currents in long wavelength infrared mercury cadmium telluride photovoltaic detectors, *J. Appl. Phys.* 116 (18) (2014) 184503.
- [6] Z.J. Quan, X.S. Chen, W.D. Hu, Z.H. Ye, X.N. Hu, Z.F. Li, W. Lu, Modeling of dark characteristics for long-wavelength HgCdTe photodiode, *Opt. Quant. Electron.* 38 (12–14) (2006) 1107–1113.
- [7] Z.J. Quan, Z.F. Li, W.D. Hu, Z.H. Ye, X.N. Hu, W. Lu, Parameter determination from resistance-voltage curve for long-wavelength HgCdTe photodiode, *J. Appl. Phys.* 100 (8) (2006) 084503.
- [8] Z.J. Quan, G.B. Chen, L.Z. Sun, Z.H. Ye, Z.F. Li, W. Lu, Effects of carrier degeneracy and conduction band non-parabolicity on the simulation of HgCdTe photovoltaic devices, *Infrared Phys. Technol.* 50 (1) (2007) 1–8.
- [9] R.S. Saxena, R.K. Bhan, R.K. Sharma, Sensitivity analysis of MWIR HgCdTe photodiodes, in: *Physics of Semiconductor Devices*, 2007. IWPSD 2007. International Workshop on. IEEE, 2007.
- [10] A. Ferron, J. Rothman, O. Gravrand, Modeling of dark current in HgCdTe infrared detectors, *J. Electron. Mater.* 42 (11) (2013) 3303–3308.
- [11] Y. Su, S. Chang, F. Juang, C. Chiang, Y. Cherng, S. Chang, Dark current mechanisms in HgCdTe photodiodes, in: *Optoelectronic Materials and Devices*. Vol. 3419. International Society for Optics and Photonics, 1998.
- [12] W.D. Hu, X.S. Chen, F. Yin, Z.J. Quan, Z.H. Ye, X.N. Hu, Z.F. Li, W. Lu, Analysis of temperature dependence of dark current mechanisms for long-wavelength HgCdTe photovoltaic infrared detectors, *J. Appl. Phys.* 105 (10) (2009) 104502.
- [13] Q. Zhi-Jue, L. Zhi-Feng, H. Wei-Da, Y. Zheng-Hua, L. Wei, Parameters extraction from the dark current characteristics of long-wavelength HgCdTe photodiode, *J. Infrared Millimeter Waves* 26 (2) (2007) 92–96.
- [14] Y. Nemirovsky, D. Rosenfeld, R. Adar, A. Kornfeld, Tunneling and dark currents in HgCdTe photodiodes, *J. Vac. Sci. Technol. A-Vac. Surf. Films* 7 (2) (1989) 528–535.
- [15] P. Martyniuk, A. Rogalski, MWIR barrier detectors versus HgCdTe photodiodes, *Infrared Phys. Technol.* 70 (2015) 125–128.
- [16] W. Qiu, W. Hu, C. Lin, X. Chen, W. Lu, Surface leakage current in 12.5  $\mu m$  long-wavelength HgCdTe infrared photodiode arrays, *Opt. Lett.* 41 (4) (2016) 828–831.
- [17] D. Blanks, J. Beck, M. Kinch, L. Colombo, Band-to-band tunnel processes in HgCdTe – comparison of experimental and theoretical studies, *J. Vac. Sci. Technol. A-Vac. Surf. Films* 6 (4) (1988) 2790–2794.
- [18] S. Singh, V. Gopal, R. Mehra, Relationship between deep levels and  $R(0)A$  product in HgCdTe diodes, *Opto-Electron. Rev.* 9 (4) (2001) 385–390.
- [19] V. Gopal, S. Gupta, R. Bhan, R. Pal, P. Chaudhary, V. Kumar, Modeling of dark characteristics of mercury cadmium telluride n<sup>+</sup>-p junctions, *Infrared Phys. Technol.* 44 (2) (2003) 143–152.
- [20] W. Peng, H. Jia-Le, X. Jiao, W. Ming-Zai, Y. Zhen-Hua, D. Rui-Jun, H. Li, Parameters extraction from the dark current characteristics of mid-wavelength HgCdTe photodiode after annealing, *J. Infrared Millimeter Waves* 36 (3) (2017) 289–294.
- [21] M. Chen, L. Colombo, J. Dodge, J. Tregilgas, The minority-carrier lifetime in doped and undoped p-type  $Hg_{0.78}Cd_{0.22}Te$  liquid-phase epitaxy films, *J. Electron. Mater.* 24 (5) (1995) 539–544.